ACS Catalysis

Research Article

Cite This: ACS Catal. 2018, 8, 6796−6809

pubs.acs.org/acscatalysis

Swellable Organically Modified Silica (SOMS) as a Catalyst Scaffold for Catalytic Treatment of Water Contaminated with Trichloroethylene

Gokhan Celik,[†] Saurabh A. Ailawar,[†] Hyuntae Sohn,[†] Yu Tang,[‡] Franklin Feng Tao,[‡] Jeffrey T. Miller,[§] Paul L. Edmiston,[∥] and Umit S. Ozkan*[,†]

[†]William G. Lowrie Department of Chemical and Biomolecular Engineering, The Ohio State University, 151 W. Woodruff Avenue, Columbus, Ohio 43210, United States

[‡]Department of Chemical and Petroleum Engineering and Department of Chemistry, The University of Kansas, Lawrence, Kansas 66045, United States

[§]Davidson School of Chemical Engineering, Purdue University, 480 Stadium Mall Drive, West Lafayette, Indiana 47907-2100, United States

[∥]Department of Chemistry, The College of Wooster, 943 College Mall, Wooster, Ohio 44691, United States

Supporting Information

ABSTRACT: The properties of a swellable organically modified silica (SOMS) scaffold allowed us to synthesize "smart" catalysts with tunable accessibility of the active sites induced by organic swelling agents. Pd nanoparticles (NPs) deposited inside the swollen matrix of SOMS were shown to be selectively located on the interior surface, a surface which is only available through swelling. Techniques such as near ambient-pressure X-ray photoelectron spectroscopy (NAP−XPS) and cryogenic scanning electron microscopy (SEM) were employed to characterize Pd/SOMS in its swollen as well as unswollen state because their conventional counterparts do not preserve the swollen state of Pd/SOMS during spectral acquisition. The results obtained depicted significant differences between the unswollen and swollen state of Pd/SOMS. The most important difference is that Pd NPs became accessible on the surface after exposure to an organic compound. This indicates that the accessibility of the active sites can be controlled by changing the reaction environment, hence allowing a tunable accessibility induced by organic swelling agents. The effects of the extent of swelling on the catalytic activity were investigated by performing catalytic activity experiments in the presence of an organic swelling agent. Hydrodechlorination (HDC) of trichloroethylene (TCE), an important method of catalytic water abatement, was chosen as a model reaction. The catalytic performance was found to be proportional to the concentration of the organic swelling agent, indicating that the accessibility of active sites is related to the concentration of organic compounds. While the unavoidable reaction product HCl inhibited the commonly used HDC catalyst 1%Pd/Al_2O_3, 1%Pd/SOMS was able to maintain its rate throughout the reaction under the same conditions, indicating its resistance to the inhibition. Overall, a silica-based catalyst with tunable accessibility of the active sites induced by changes in the reaction environment can have significant implications for heterogeneous catalysis.

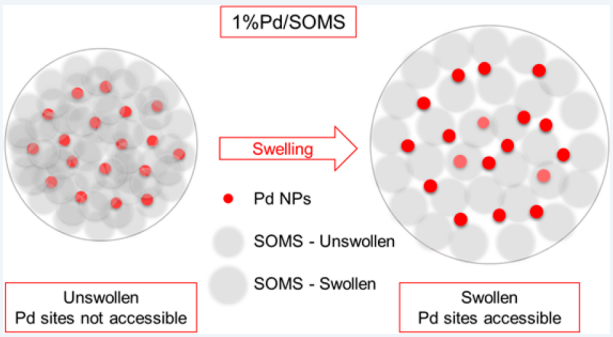

KEYWORDS: *swellable organically modified silica (SOMS), organosilicate, swelling, smart catalytic materials, stimuli-induced materials, hydrodechlorination, trichloroethylene*

1. INTRODUCTION

Animated materials are a class of materials whose characteristics exhibit stimuli-induced responses where the stimuli are pH,[1−4] temperature,[5,6] or exposure to organics in the gas, liquid, or solid phase.[7−11] The development of such materials opens opportunities for engineering heterogeneous "smart catalysts" with improved activity, selectivity, and resistance to deactivation. There is a variety of animated materials reported in the literature including hyper-cross-linked polymers,[7,8,12,13] hydrogels,[1−,3,1415] and swellable organically modified silica (SOMS).[9−11,16−20] Unlike conventional catalytic supports such as silica, carbon, or alumina, the animated materials do not have an inelastic structure with a constant porosity under working conditions.

Hyper-cross-linked polymeric materials are one of the earliest type of animated materials that have benzene-ring

Received: April 30, 2018
Revised: June 6, 2018
Published: June 8, 2018

DOI: 10.1021/acscatal.8b01700
ACS Catal. 2018, 8, 6796−6809

containing groups such as divinylbenzene and styrene in their structure. When hyper-cross-linked polymers are synthesized in the presence of a solvation diluent, solvent, and a cross-linking agent, copolymerization of monomers creates a polymeric network with divinylbenzene bridges. During copolymerization, phase separation takes place, and two phases form: the cross-linked polymer and the solvent. Upon the removal of the solvent by evaporation, a cross-linked polymer is obtained. Depending on the type of the cross-linking agent and degree of cross-linking, the resulting material may have conformational mobility and exhibit swelling upon contact with water or organics.[7,8,12,13] In addition, hydrogels prepared from polymeric precursors exhibit pH-dependent swelling behavior upon contact with water. The use of such materials for drug delivery purposes was studied.[1,3,15,21] Since hydrogels are hydrophilic in nature, their applicability to catalysis and adsorption may be limited because the hydrophilicity of hydrogels may limit the efficiency of the extraction of dissolved organics from water.[9] In addition, the hydrophilicity of hydrogels may lower the resistance to deactivation due to anionic groundwater poisons when used for catalytic treatment of water.

Any material which has an organic bridge within the structure connected to a benzene ring is a candidate material to exhibit stimuli-induced swelling behavior.[13] However, finding the right conditions to synthesize such materials requires many experimental studies. Edmiston and co-workers developed a well-defined set of synthesis conditions to obtain a swellable organo-silica material (SOMS) derived from a matrix of cross-linked polysilsesquioxanes.[9−11] SOMS was synthesized by polycondensation of alkoxysilane monomers in a solvent via the sol−gel process. An organic−inorganic network was formed through the formation of a colloidal suspension and gelation of the suspension. A three-dimensional porous siloxane network was obtained after polymerization, followed by several chemical steps including hydrolysis, alcohol condensation, and water condensation. After the gelation, the solvent was removed by evaporation.[9−11]

The siloxane-based network of SOMS has a benzene ring with an aryl group which acts as an organic bridge and gives it a flexibility to swell rapidly upon contact with organic compounds. The unswollen matrix of SOMS is under a tensioned-state due to tensile forces generated and stored by the capillary-induced collapse of the matrix upon drying during synthesis. The organic compounds disrupt noncovalent interactions, causing a subsequent release of the tensile energy stored by distortion of a collapsed pore structure on drying. SOMS has a highly cross-linked network that retains its flexibility to expand and contract upon exposure to organic liquids. When conventional mesoporous silica is exposed to organic compounds, either its structure undergoes irreversible damages due to fracturing during the solvent removal step or the degree of cross-linking may increase due to additional Si−O−Si formation. It has been reported that swelling is highly dependent on sol−gel synthesis conditions and can only be produced under a narrow set of experimental parameters. Because of its hydrophobic nature, SOMS does not swell when exposed to water, but it swells when exposed to organic compounds.[9−11] SOMS is thermally more stable than other polymeric animated materials because of its organosilicate structure. Therefore, SOMS, among other animated materials, has more potential to be used as a catalyst scaffold.

The uses of animated materials as catalytic scaffolds were not exploited despite their novel characteristics. We hypothesize that if active sites can be incorporated into the swollen matrix of SOMS, deactivation resistance of solid-catalyzed reaction system could be significantly improved. Considering that catalytic water treatment systems including, but not limited to, hydrodechlorination, hydrogenation, and defluorination reactions suffer from deactivation issues, the prospects of using a deactivation-resistant catalyst such as Pd/SOMS would be high. The key for development of poison-resistant catalyst, however, resides in SOMS' ability to exhibit stimuli-induced behavior during Pd-incorporation in synthesis and under reaction conditions. The accessibility of Pd NPs deposited inside the swollen matrix of SOMS is expected to strongly depend on the extent to which SOMS swells. For this reason, investigations are needed to confirm that active metals can be selectively located in the swollen matrix of SOMS, and the accessibility of Pd NPs can be altered by the reactive environment under working conditions.

Aqueous-phase hydrodechlorination (HDC) of trichloroethylene (TCE) was chosen as a model reaction to demonstrate catalytic performance of Pd-incorporated SOMS in its unswollen and swollen state. HDC is one of the widely studied reactions from applied and fundamental catalysis point of view. It is an elimination-based remediation technique in which chlorinated compounds react with H_2 and are catalytically converted to chloride-free hydrocarbons and HCl. There has been ongoing research on HDC of chlorinated compounds where promising conversions and catalytic activities were obtained with the palladium-based state-of-the-art catalysts.[22−32] The existing hydrodechlorination catalysts reported in the literature, however, suffer from catalyst poisoning due to anionic species present in real groundwater, inhibition by the unavoidable reaction product HCl, the formation of carbonaceous species on active sites, and active metal leaching.[24,25,33−43] In our present contribution, studies were performed to confirm whether active metals can be selectively located in the swollen matrix of SOMS and to understand the behavior of the active sites with respect to different reactive environments. Catalytic activity experiments and characterization studies were performed to examine properties of SOMS and Pd-incorporated SOMS in their unswollen and swollen states. The challenges of keeping SOMS and Pd/SOMS in the swollen form during spectral acquisition were overcome by use of advanced characterization techniques such as NAP−XPS, cryogenic SEM, and in situ X-ray absorption spectroscopy.

2. EXPERIMENTAL SECTION

2.1. Catalyst Synthesis. The synthesis procedure of SOMS scaffold was reported previously by Edmiston and his co-workers.[9−11] Palladium was impregnated to SOMS thorough incipient wetness impregnation (IWI) technique. In a typical synthesis, Pd(II) acetate (Sigma-Aldrich 99.9%) was dissolved in acetone and then added dropwise to the SOMS until Pd-containing solution saturated the scaffold. The saturated SOMS was dried at room temperature. The saturation and drying steps were repeated until all the precursor solution was consumed. The resulting Pd/SOMS catalyst was first reduced by $NaBH_4$ dissolved in 95% ethanol solution, washed with ethanol, and dried at 70 °C overnight. In addition, 0.5%Pd/Al_2O_3 and 1%Pd/Al_2O_3 catalysts were purchased from Sigma-Aldrich and reduced at 350 °C with H_2.

2.2. Nitrogen Physisorption. Nitrogen physisorption experiments were performed at 77K on an accelerated surface

DOI: 10.1021/acscatal.8b01700
ACS Catal. 2018, 8, 6796−6809

area and porosimetry instrument (ASAP-2020, Micromeritics). Prior to analysis, catalysts were degassed at 120 °C and 2 μmHg for 12 h to remove moisture and adsorbed gases. The surface area of catalysts was determined by the Brunauer–Emmett–Teller (BET) method at the relative pressure (P/P_0) range of 0.06–0.2. The pore volume and pore size of the catalysts were determined by the Barrett–Joyner–Halenda (BJH) method from the amount desorbed at the relative pressure of 0.984. The pore size distribution of catalysts was also determined by applying the BJH method to the desorption isotherm. In order to assess the microporosity of SOMS and 1%Pd/SOMS, α_s-plot analysis was performed by following the procedure reported by Jaroniec et al. and using standard reduced nitrogen adsorption data for LiChrospher Si-1000, a macroporous silica reference material.[44]

2.3. Static Vapor-Phase Adsorption. Static vapor equilibrium adsorption experiments were performed at 25 °C using Pyris 1 PerkinElmer thermogravimetric analyzer. A certain amount of sample, SOMS scaffold, or 1%Pd/SOMS catalyst, in powder form, was placed in the analyzer and weighed under dry air. A static condition of saturated vapor was created by adding 5 mL of liquid acetone or water, inside the sealed 50 mL chamber of the thermogravimetric analyzer, thus allowing SOMS materials to be continuously exposed to gas phase water or acetone. The changes in the mass of the SOMS materials upon exposure to acetone or water vapor were recorded over time until equilibrium was reached.

2.4. CO Pulse Chemisorption. Chemisorption experiments were performed in pulse mode using CO as a probe molecule to obtain information about the accessibility of Pd NPs to the probe molecule. Experiments were performed in a homemade chemisorption system which is equipped with a six-port valve having a sample loop for CO injection, mass flow meters to create the desired gas environments, a Carbolite MTF 10/15/130 furnace, and a mass spectrometer (MS) (MKS − Cirrus II) operated in scanning ion mode. A certain amount of catalyst was placed in a 4 mm-ID quartz reactor and supported by quartz wool plugs. Then, the reactor was positioned at the center of the furnace and the exit stream was connected to the MS where concentration of m/z = 28 signal was monitored throughout the experiment.

1%Pd/SOMS and 1%Pd/Al_2O_3 catalysts were used as described in Section 2.1. Prior to CO injections, catalysts were pretreated at 110 °C for 1 h under 30 ccm He flow to remove moisture and weakly bound CO_2. After the pretreatment step, temperature was reduced to 40 °C. Once the temperature and MS signals were stable, CO pulses were sent to the catalyst bed. The total amount of CO uptake at each pulse was calculated by calibrating the MS for a pulse of CO through the empty bed.

2.5. DRIFTS of Adsorbed CO. The interactions of adsorbed CO with Pd-incorporated SOMS was examined through in situ diffuse reflectance Fourier transform spectroscopy (DRIFTS) at 40 °C. Thermo NICOLET 6700 FTIR spectrometer equipped with a cryogenic MCT detector and KBr beam splitter was used. 1%Pd/SOMS in powder form was grinded and loaded into the sample chamber of an in situ reaction cell (Praying Mantis, Harrick Scientific Products, Pleasantville, New York) in which the gaseous environment and temperature can be controlled. Before CO adsorption, the cell was flushed with He at room temperature, pretreated at 110 °C, and cooled to 40 °C under 30 ccm He. A background spectrum was collected at this temperature before introducing CO to the cell. CO was adsorbed on the sample for 30 min. Once the adsorption was over, the gas flow was switched to He and the spectrum was acquired after the gas phase CO was flushed with He. The spectrum consisted of 450 scans at 4 cm^{-1} resolution. The background spectrum collected before CO adsorption was subtracted from the sample spectrum by using OMNIC 8.1 software.

2.6. X-ray Photoelectron Spectroscopy. XPS experiments were carried out in a Kratos Ultra Axis Spectrometer equipped with a monochromatized Al Kα X-ray source operating at 12 kV and 10 mA. Powder samples were loaded on a carbon tape and placed in the XPS chamber. After evacuation overnight, a survey scan followed by high resolution region scans were collected. The depth profiles of Pd-incorporated SOMS was investigated by sputtering the top layers of the surface with an Ar^+-ion gun operating at 3 kV. The charging effects were corrected with respect to C 1s (284.5 eV). Deconvolution and data analysis were performed by using CasaXPS 2.3.16 software.

2.7. Near Ambient Pressure–X-ray Photoelectron Spectroscopy (NAP–XPS). The changes in the Pd 3d region upon exposure to ethanol vapor were investigated with an in-house NAP–XPS using monochromatized Al Kα X-ray.[45−47] Two NAP–XPS experiments were performed. In the first experiment, Pd/SOMS was deposited on a carbon tape without any solvent. The spectrum was acquired under UHV at 25 °C. In the second experiment, Pd/SOMS was mixed with ethanol to induce swelling and immobilized on carbon tape. The sample holder was placed in the chamber and excess ethanol was vaporized at 60 °C. The temperature was reduced to 25 °C, and a spectrum was collected. Both spectra were calibrated with respect to C 1s at 284.5 eV.

2.8. Time-Resolved X-ray Absorption Near Edge Structure (XANES) Spectroscopy—Aqueous-Phase In Situ Reduction of Pd. An aqueous-phase in situ XAFS reactor system was built to study the reduction behavior of Pd in preoxidized 1%Pd/SOMS and 1%Pd/Al_2O_3 catalysts at room temperature and atmospheric pressure. The design details and operating procedures of the in situ XAFS reactor described by Kispersky et al.[48] and Fingland et al.[49] were followed with some modifications. Deionized water saturated with H_2 was sent to the XAFS reactor at a flow rate of 1 mL/min. The reactor dimensions were decided after calculating the transmittance of several tubes with different wall thicknesses and outside diameters. On the basis of the calculations, an NMR tube with an OD of 0.197 in. and ID of 0.167 in. was used, resulting in an absorbance of 0.25 due to reactor and 3.20 due to catalyst at the Pd K edge. The NMR tube was fused to a 0.25 in quartz tube on both ends and connected to the system by using O-ring seals and vacuum connections. A known amount of catalyst was grinded, loaded into the reactor, and supported from both sides with quartz wool plugs.

Palladium K edge (24.350 keV) X-ray absorption fine structure (XAFS) measurements in transmission mode were performed on the insertion device beamline of the Materials Research Collaborative Access Team (MRCAT-10ID) at Advanced Photon Source at Argonne National Laboratory. Measurements were performed in quick-scan mode. A cryogenically cooled double-crystal Si(111) monochromator was used with a Pt-coated mirror to minimize the presence of harmonics. The spectrum reproducibility was ensured by obtaining multiple scans before the time-resolved reduction experiment. A Pd foil spectrum was acquired simultaneously

DOI: 10.1021/acscatal.8b01700
ACS Catal. 2018, 8, 6796–6809

with each measurement for energy calibration. The Pd edge energy was determined as the position of the maximum of the first peak in the first derivative of the XANES region. Average oxidation state of Pd NPs was obtained by fitting the XANES spectra as a linear combination of the spectra for the prereduction and postreduction samples, oxidation states of which were obtained using the EXAFS analysis. The Athena software was used for the XANES analysis.[50] Standard procedures were followed to extract EXAFS data by using WINXAS 3.2. software.[51] Phase shifts and backscattering amplitudes were obtained experimentally from EXAFS spectra of Pd foil for Pd−Pd (12 at 2.75 Å) and palladium oxide for Pd−O (4 at 2.05 Å). The EXAFS coordination parameters (*N*: coordination number and *R*: bond distance) were obtained by a least-squares fit in R-space and k-space of the nearest neighbor.

2.9. Cryogenic Scanning Electron Microscopy. The morphological changes of samples upon swelling were characterized by cryogenic scanning electron microscopy using Helios 600 operating at an accelerating voltage of 5 kV. The SEM was equipped with a cryogenic stage (Quorum PP3010) for low-temperature SEM imaging. SOMS and Pd/SOMS catalysts in their powder form were mixed with a few drops of ethylene glycol to induce swelling. Ethylene glycol-containing samples along with their dry counterparts were placed on a sample holder and transferred into cryo-preparation chamber where the samples were first cooled to 133 K and then pumped down to vacuum. After coating the samples with Pt, the sample holder was transferred into the SEM chamber where the ethylene-glycol containing samples remained swollen during imaging.

2.10. Catalytic Activity Experiments. Aqueous-phase HDC of TCE experiments were performed over Pd/SOMS and Pd/Al_2O_3 at 50 bar and 30 °C, unless otherwise stated. The autoclave reactor was loaded with 200 mL of starting solution containing 1000 ppm TCE. Experiments were also performed in the presence of 1% or 10% ethanol in the reaction solution. A known amount of catalyst was loaded to the catalyst addition device and secured in the headspace of the reactor. Before H_2 introduction, the reactor was flushed with He to eliminate the presence of O_2 in the reactor. Once the flushing was over, and the temperature was stable at 30 °C (the lowest reaction temperature that can be accurately controlled throughout the reaction), the reactor was pressurized up to 50 bar to ensure the presence of excess H_2, providing a molar ratio of H_2 to TCE higher than 10. Moreover, there is a pure-H_2 headspace over the reaction solution forming a sufficient reservoir of H_2.

Before the introduction of catalyst to the reaction solution, a liquid sample was taken from the reactor to determine the initial concentration of TCE. The initial concentration of TCE was found to be approximately 250 ppm. The activity experiments were performed with high initial concentrations of TCE, which may be more relevant to wastewater treatment systems, the activity results can be informative for groundwater treatment systems as well where TCE concentrations are typically low[52] The catalyst addition device was activated to start the reaction and liquid samples were taken throughout the reaction at periodic intervals via a 1/16 in. OD sampling tube that extends to the bottom of the reactor. The sampling tube has a filter which keeps the catalyst particles inside the reactor while sampling. It is attached to an airtight vial from which samples were taken with a gastight syringe.

The liquid samples taken from the reactor were analyzed using HPLC equipped with a UV−vis detector (Shimadzu, SPD-20A). The HPLC was operated in binary-mode phase where the mobile phase is 50% acetonitrile and 50% water. The mobile phase underwent gradient elution to 95% acetonitrile and 5%water during the analysis. The analysis, separation, and quantification of Cl-containing products and unconverted educts were achieved with the help of an injection loop with a known volume, an injection valve, and C18 column as well as using tetrahydrofuran as a standard.

The concentration of HCl was measured with a selective chloride electrode (Cole Palmer, UX-27504-08). Chloride balance was performed to ensure the mass balance of the system. A chloride balance of 96% or higher was obtained indicating the accuracy of the measurements and confirming that undetected Cl-containing species or loss of volatile compounds during the reaction was negligible. The selectivity (S_i) of chloride-containing products was calculated by using eq 1.

$$S_i(t) = \frac{a_i \times n_i(t)}{3(n_{TCE}(t=0) - n_{TCE}(t))} \quad (1)$$

where a_i is the number of chloride atoms present in the product i, $n_{TCE}(t)$ is moles of TCE in the reactor at time *t*. For instance, for 1,1-DCE, cis-1,2-DCE, and trans-1,2-DCE, a_i is equal to two, whereas for vinyl chloride and HCl, a_i is equal to one.

It should be noted that the operating parameters used in this study including high pressure and use of ethanol to swell Pd/SOMS are not directly applicable to catalytic water treatment systems. 50 bar was chosen as the operating pressure to perform HDC experiments in excess H_2. Ethanol was chosen as an organic swelling agent to demonstrate the changes in the catalytic activity and accessibility of Pd NPs on SOMS.

3. RESULTS AND DISCUSSION

3.1. Characterization of SOMS and Pd/SOMS. *3.1.1. Nitrogen Physisorption.* Nitrogen physisorption experiments were performed to examine the textural properties of SOMS and the changes therein upon Pd incorporation. Textural properties, surface area as determined by the BET method, and average pore volume and average pore size, as determined from BJH desorption isotherm, of SOMS and 1% Pd/SOMS are shown in Table 1. Incorporation of Pd to SOMS did not change the surface area significantly. There were, however, notable decreases in the average pore volume and the average pore diameter due to Pd incorporation.

Table 1. Textural Properties of SOMS and 1%Pd/SOMS

samples	BET surface area, m^2/g	pore volume, cc/g	pore diameter, nm
SOMS	614	0.94	5.4
1%Pd/SOMS	590	0.73	3.9

BJH pore-size distribution plots and nitrogen adsorption−desorption isotherms of SOMS and Pd-incorporated SOMS are shown in Figure 1. When pore size distributions were examined, it can be seen from Figure 1a that BJH pore size distribution of SOMS is centered around three peaks at 3.8, 6.3, and 11.2 nm, and that of Pd/SOMS is centered around 3.7 and 5.4 nm. The peaks at 3.8 and 3.7 nm in the pore size distribution of SOMS and 1%Pd/SOMS are due to artifacts of

DOI: 10.1021/acscatal.8b01700
ACS Catal. 2018, 8, 6796−6809

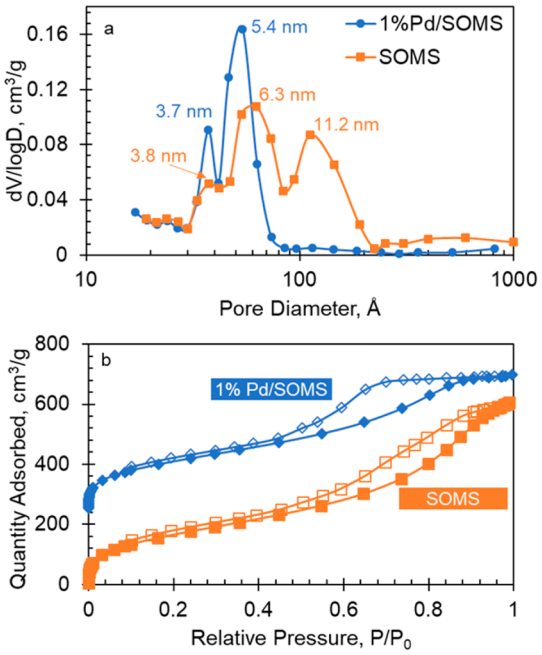

Figure 1. (a) BJH pore size distributions and (b) N_2 adsorption–desorption isotherms of SOMS and Pd-incorporated SOMS.

nitrogen adsorption measurements and will be discussed in more detail later in the manuscript. SOMS exhibited a bimodal porous structure with small pores at 6.3 nm and large pores at 11.2 nm. Fuertes et al. characterized the small mesopores as structural mesopores and the larger mesopores as complementary mesopores, which formed during sol–gel synthesis after the syneresis step.[53,54] In addition, pores larger than 30 nm were also noted in the pore size distribution plot of SOMS. The wide nature of the pore size distribution of SOMS suggests that the porous structure is not well-ordered.[53] Pd-incorporation changed the pore size distribution significantly. The bimodal porous structure of SOMS turned into a unimodal porous structure with pore size distribution centered at 5.4 nm. The pore size of the small pores of SOMS decreased from 6.3 to 5.4 nm upon Pd incorporation. The most plausible explanation for the shrinkage of the smaller pores is the Pd deposition on the walls of the pores. No peaks were noted at large pore diameters, indicating that the complementary pores observed over SOMS were lost after Pd impregnation. This could be attributed to pore blocking by large Pd clusters.

Adsorption–desorption isotherms of both samples, shown in Figure 1b, exhibited monolayer adsorption of nitrogen at low relative pressures where P/P_0 is less than 0.2 and type-IV isotherm with a hysteresis caused by capillary condensation of N_2 over a wide relative pressure range, both of these are characteristics of mesoporous materials.[55] The hystereses observed on SOMS and 1%Pd/SOMS are, however, different in nature indicating that structural differences exist in the porous network of SOMS and 1%Pd/SOMS. According to IUPAC's hysteresis classification, hystereses of SOMS and 1% Pd/SOMS can be characterized as H4 and H2, respectively.[55] The disappearance of the complementary pores due to Pd impregnation was also confirmed by comparing the isotherms of SOMS and Pd/SOMS. Unlike SOMS, the hysteresis observed over Pd/SOMS did not extend to higher relative pressures due to the absence of larger mesopores. Large pores are typically filled at high relative pressures around 0.9.[56,57]

The broad nature of the hysteresis observed over SOMS is a direct consequence of the bimodal porous network and swellable nature. The observed H4-type hysteresis occurred because of bimodal porous structure, and additionally, the adsorption and desorption branches of the isotherm did not overlap at low P/P_0 values, indicating the presence of a distinct hysteresis. This type of hysteresis is called sorption hysteresis and is observed in swellable materials such as hyper-cross-linked polystyrenes.[12] The onset of H4-hysteresis, however, can be considered as the relative pressure of 0.45, where the magnitude of hysteresis increased prominently compared with lower relative pressures. The corresponding forced closure observed around P/P_0 = 0.45–0.50 on the desorption isotherm is an indication of tensile strength effects and has been reported to cause a peak around 4 nm in the pore size distribution plot.[58] The desorption branches shown in Figure 1b, particularly that of Pd/SOMS, exhibited such a feature with a corresponding peak at 3.7 nm in the pore size distribution plot. Groen et al. reported an approach to figure out whether the peak obtained around 4 nm is a real feature or an artifact of gas adsorption measurements.[58] As per the approach, the pore size distributions obtained from the desorption branch and the adsorption branch of the isotherm were compared to see whether both distributions exhibit similar peaks. A peak originating from the tensile strength effect appears on the pore size distribution plot obtained from the desorption branch of the isotherm, but it does not appear on the pore size distribution obtained from the adsorption branch because the latter is not subject to tensile strength effects.[58] The comparison revealed that the peak at 3.8 nm for SOMS and the peak at 3.7 nm for 1%Pd/SOMS were due to artifacts of gas-adsorption measurements and do not originate from the existence of real pores.

In order to assess whether micropores are present in SOMS, the α_s-plot (shown in Figure S1) was created by using the standard reduced nitrogen adsorption isotherm data for LiChrospher Si-1000 macroporous silica.[44] A linear α_s-plot was obtained at standard reduced adsorption values less than 1.0, indicating the absence of detectable amount of microporosity in SOMS. In addition, the upward deviation from the linear behavior in the capillary condensation region ($\alpha_s \sim 2$) and the amount of adsorbed nitrogen reaching to a stable level at higher standard reduction values are consequences of nitrogen adsorption on the mesoporous structure of SOMS. The linear relation obtained at low standard reduced adsorption data could also be attributed to similar adsorption energy of nitrogen on SOMS and LiChrospher Si-1000 macroporous silica. This is of importance because SOMS contains organic functional groups and these groups do not have a significant effect on the adsorption energy of nitrogen.[44]

At this point, it is beneficial to note that the BET method is unable to measure the "true" surface area of SOMS and 1%Pd/SOMS. The inherent difficulty is that these animated materials do not have an inelastic structure with constant properties such as surface area, pore diameter, and porosity under reaction conditions. As mentioned in the Introduction, SOMS is an animated catalytic scaffold whose volume expands upon exposure to organic chemicals. The swelling process enhances its surface area, pore volume, and pore size. SOMS returns to its unswollen state upon removal of the swelling agent because the swelling process is reversible.[9–11,19,20] The fact that SOMS cannot be kept at its swollen state due to the lack of an organic swelling agent during nitrogen physisorption measurement

DOI: 10.1021/acscatal.8b01700
ACS Catal. 2018, 8, 6796–6809

results in measuring the surface area of SOMS at its unswollen-state. The surface area and pores which would be generated upon swelling are inaccessible to nitrogen during N_2 physisorption experiment. The inaccessible pores cannot be detected by nitrogen physisorption. Similar problems were experienced by other researchers as well when dealing with swellable hyper-cross-linked polymer-based animated materials.[13] Therefore, it can be stated that the textural properties obtained by nitrogen gas adsorption experiment underestimates the available surface area and pore dimensions of SOMS and Pd/SOMS.[13]

3.1.2. Static Vapor-Phase Adsorption Measurements. Static vapor-phase adsorption experiments were performed to determine the changes in the hydrophobicity and adsorption capacity of SOMS scaffold due to Pd incorporation, by using water vapor and acetone vapor, respectively. The percent increase in the mass of SOMS and Pd-incorporated SOMS with respect to exposure time of acetone vapor and water vapor are shown in Figure S2. At equilibrium, acetone uptake of SOMS was found to be 38 times the amount of water adsorbed on SOMS. These uptake values are expected because SOMS has high affinity for adsorbing organics while repelling water vapor due to its hydrophobicity.[10,11,18] Upon Pd incorporation, acetone adsorption behavior did not change significantly, if anything somewhat increased. Pd-incorporation increased the amount of water adsorbed. However, the material still retained a high hydrophobicity, exhibiting an equilibrium ratio of acetone uptake to water uptake of around 7.[18,19]

3.1.3. CO Pulse Chemisorption. CO was used as a probe molecule to perform pulse chemisorption experiments with the aim of obtaining the amount of CO uptake and information about the accessibility of Pd NPs deposited on SOMS. CO was introduced to the reactor bed by pulses. The evolution of m/z = 28 signal through mass spectrometer is shown in Figure 2.

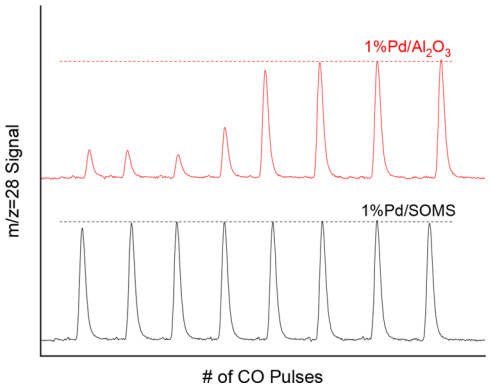

Figure 2. CO pulse chemisorption over 1%Pd/SOMS and 1%Pd/Al_2O_3. CO uptake was monitored by mass spectrometer signal m/z = 28.

Each pulse corresponds to a feed of 1.22 mmol of CO. The pulse chemisorption profile of 1%Pd/SOMS is interesting and unconventional. Except a slight CO uptake in the first pulse corresponding to 0.04 mmol/mgPd, no CO uptake was observed during additional pulsing. The bare SOMS did not exhibit any measurable CO uptake indicating that the CO uptake is primarily due to the interaction of the probe molecule with Pd. Experiments were also performed over commercially available HDC catalyst 1%Pd/Al_2O_3. As observed in Figure 2, partial uptake of the first five CO pulses occurred on 1% Pd/Al_2O_3. From the sixth pulse onward, no change in the m/z = 28 signal was noted indicating that all available Pd sites were occupied by adsorbed CO. The total amount of CO uptake was found to be 3.71 mmol/mgPd.

The CO uptake over Pd/Al_2O_3 was significantly higher than Pd/SOMS, although both samples contained the same amount of the active metal. The observed difference was attributed to the fact that Pd sites were deposited inside the swollen matrix of SOMS during synthesis. In other words, during CO pulse chemisorption studies, Pd/SOMS was in its closed state where Pd NPs were not accessible on the exterior surface. On the surface that CO pulses can access, there is a very little presence of surface Pd as shown by Pd 3d XPS spectrum as explained in Section 3.1.5. The CO uptake observed over the first pulse was attributed to the Pd which is on the exterior surface. Additionally, CO may be too polar to enter the pores of Pd/SOMS due to its hydrophobicity. For these reasons, it is very difficult to determine dispersion for Pd/SOMS materials by sorption techniques because experimental conditions required by these techniques will keep Pd/SOMS in its unswollen state.

3.1.4. DRIFTS of Adsorbed CO. Infrared spectroscopy of CO adsorbed on metal surface sites reveals information about the nature of supported metal catalysts.[59−65] Pd-incorporated SOMS was studied with DRIFTS by using CO as a probe molecule to gain insight into the properties of Pd incorporated to SOMS. For this purpose, Pd/SOMS was saturated with CO and purged with He to remove weakly bound carbonyl species. The infrared spectrum of Pd/SOMS between 2300 and 1800 cm^{-1} is shown in Figure 3. There are three distinct bands

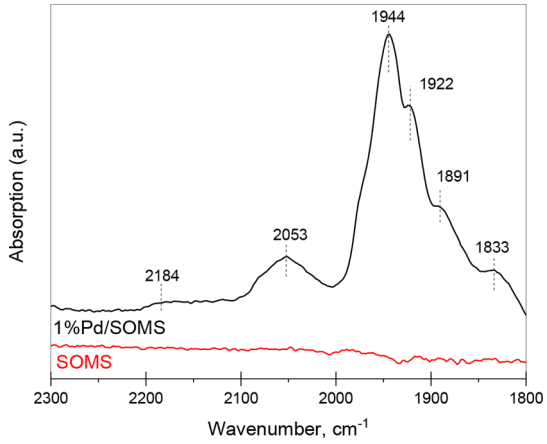

Figure 3. DRIFTS spectra of CO adsorbed at 40 °C on 1%Pd/SOMS after flushing with He.

observed at 2184, 2053, and 1944 cm^{-1} which has other features on the shoulder at lower wavenumbers. The wavenumber region above 2000 cm^{-1} contained IR bands associated with CO adsorption on SOMS and linearly adsorbed CO on oxidized Pd and metallic Pd. The weak band at 2184 cm^{-1} could be attributed to interactions of CO with the SOMS scaffold which contains Pd sites. On alumina supports, such a band that appears between 2200 and 2186 cm^{-1} was attributed to interactions of CO with coordinately saturated (cus) Al^{3+} sites.[60] IR bands above 2100 cm^{-1} is ascribed to CO adsorbed on cationic Pd.[59,60] No such bands were observed indicating that Pd is in metallic state. The 2053 cm^{-1} band was attributed to CO linearly adsorbed on Pd.[60,61]

DOI: 10.1021/acscatal.8b01700
ACS Catal. 2018, 8, 6796−6809

The 1944 cm^{-1} band along with the bands at 1925−1830 cm^{-1} were ascribed to 3-fold bridged CO on Pd in different adsorption environments.[60,62,66] CO adsorption with DRIFTS experiment was also performed on bare SOMS to verify that these peaks are indeed due to adsorption of CO on Pd.

It has been reported that the position of the carbonyl bands depends on factors such as particle size of Pd and surface coverage of CO.[63−65] The low ratio of linearly adsorbed CO to bridged adsorbed CO and lower IR band positions for these adsorption groups can be explained by low Pd dispersion on Pd/SOMS[16] and marginally low CO uptake on Pd/SOMS as shown by pulse chemisorption experiments in Section 3.1.3. Pd-containing samples with high dispersion and CO surface coverage exhibit an IR band at 2090 cm^{-1} due to linearly adsorbed CO.[60] As Pd particle size increases and surface coverage decreases, the band at 2090 cm^{-1} and bands due to bridged CO shift to lower wavenumbers because of changes in dipole−dipole interactions.[62] It is also possible that SOMS as a scaffold may create a synergic effect which may increase palladium d-orbital electron availability of Pd/SOMS to back-donate to $2\pi^*$ antibonding vacant orbital of CO.[59,63]

3.1.5. X-ray Photoelectron Spectroscopy and Surface Sputtering. Pd NPs deposited on SOMS were characterized by X-ray photoelectron spectroscopy. XPS is a characterization technique which only probes the surface.[67] Since Pd NPs were embedded inside the swollen matrix of SOMS during synthesis, no Pd is expected to appear on the surface. For this purpose, XPS experiments are performed to assess whether Pd is on the surface or in the bulk of SOMS. The spectrum of Pd 3d region is shown in Figure 4. As shown in the figure, a horizontal line

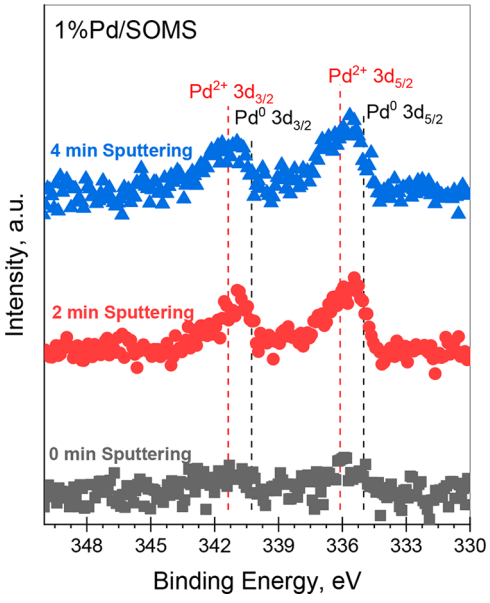

Figure 4. XPS spectra of Pd 3d region of 1%Pd/SOMS upon Ar^+-ion sputtering for different durations.

with a very weak Pd signal was obtained in the spectrum, indicating that Pd is not on the exterior surface of SOMS. It also implies that the incorporation of Pd to the swollen matrix of SOMS was successful.

The top layers of the surface were removed by Ar ion sputtering to obtain a depth profiling of Pd NPs deposited on SOMS. The sputtering was performed for 2 minutes followed by 2 additional minutes to see the evolution of Pd 3d signal. As the surface was sputtered, an increase in the Pd signal was noted, indicating that Pd NPs appeared on the surface as the top surface layers were removed. The results also confirm that Pd was deposited inside the matrix of SOMS.

3.1.6. Time-Resolved X-ray Absorption Near Edge Structure (XANES) Spectroscopy—Aqueous-Phase In Situ Reduction of Pd. The reducibility of Pd NPs supported on Al_2O_3 and SOMS was examined by time-resolved in situ XANES spectroscopy. The reduction of Pd was performed in aqueous-phase with H_2-saturated water at room temperature and atmospheric pressure. The XANES spectra were fitted by using prereduction and postreduction spectra of the samples as references. The reduction profiles of Pd/Al_2O_3 and Pd/SOMS together with k2-weighted Fourier transform magnitudes of EXAFS spectra of prereduction and postreduction samples of Pd/Al_2O_3 and Pd/SOMS are shown in Figure 5. The reduction profile shows that both samples were reduced. However, the extent of reduction within 2 hours and the reduction kinetics were different over Pd/Al_2O_3 and Pd/SOMS. At the end of 60 min of reduction, the average oxidation state of Pd NPs on Pd/Al_2O_3 was found to be 0, whereas that on Pd/SOMS was found to be 0.8. Furthermore, the changes in the fraction of oxidized Pd NPs were fitted to a first-order power law type rate expression. The reduction profiles were successfully fitted (R^2 = 0.97) as shown in the inset of Figure 5a, indicating that the reduction mechanism over both samples are similar. The reduction rate constant, obtained from the slope of natural logarithm of the fraction of oxidized Pd NPs vs time plot, was 0.137 and 0.014 min^{-1} for Pd/Al_2O_3 and Pd/SOMS, respectively.

The fitting results of the reference spectra used in XANES analysis are shown in Table S1. The prereduction samples were completely oxidized. After in situ reduction with water saturated with H_2, a metallic-state of Pd NPs was obtained over Pd/Al_2O_3, while approximately 20% of Pd NPs were found to be in 2+ oxidation state over Pd/SOMS. The Pd−Pd bond distances of Pd NPs over Pd/Al_2O_3 and Pd/SOMS were found to be slightly longer than 2.75 Å (Pd−Pd bond distance in Pd foil). This was attributed to the formation of Pd−H that is typically observed when Pd NPs are in contact with H_2 at room temperature.[68,69] The formation of Pd−H during aqueous-phase reduction suggests that Pd may also exist in hydride form under HDC of TCE reaction conditions.

The average Pd NP size can be estimated from the Pd−Pd coordination number.[70] For 1% Pd/Al_2O_3, a coordination number of 8.8 gives a particle size of about 4 nm. For 1% Pd/SOMS, the fit Pd−Pd coordination number is 5.6. However, this sample is partially oxidized (e.g., about 20% Pd^{2+} and 80% metallic Pd). The fit coordination number divided by the fraction of metallic Pd gives the true coordination number, or 7.0, which is consistent with Pd NPs of about 2.5 nm.

3.2. Characterization Studies Performed in the Presence of an Organic Swelling Agent. *3.2.1. Near Ambient Pressure−X-ray Photoelectron Spectroscopy (NAP−XPS).* As explained in the Introduction, Pd/SOMS is an animated material where the accessibility of Pd NPs may change as a function of the reaction environment. Pd signal was not obtained in XPS measurements under UHV, as reported in Section 3.1.5, because photoelectrons originating from Pd NPs could not escape from the matrix and lost their intensity before reaching the detector. If Pd/SOMS could be maintained in its swollen state during XPS data acquisition, photoelectrons originating from Pd NPs may be able to escape

DOI: 10.1021/acscatal.8b01700
ACS Catal. 2018, 8, 6796−6809

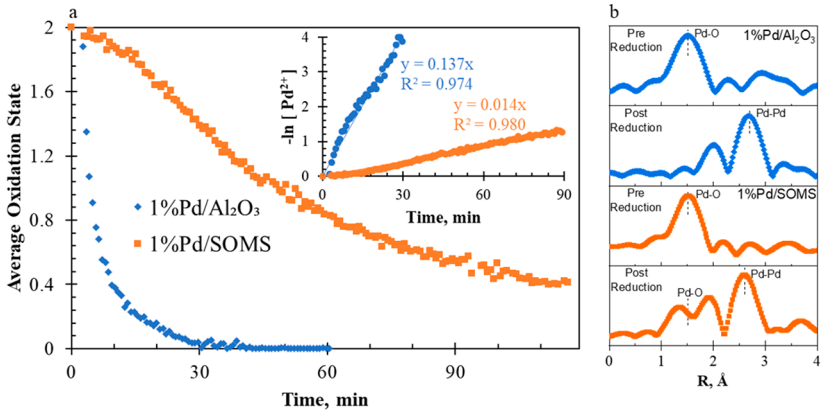

Figure 5. (a) Average oxidation state of Pd obtained from time-resolved in situ XANES spectra over preoxidized Pd/SOMS and Pd/Al_2O_3. Inset: plots of natural logarithm of the fraction of oxidized Pd NPs versus time over 1%Pd/SOMS and $1\%Pd/Al_2O_3$. The slope indicates the reduction rate constant. (b) The k2-weighted Fourier transform (FT) magnitudes of prereduction and postreduction samples of $1\%Pd/Al_2O_3$ and 1%Pd/SOMS.

through the swollen matrix without losing its energy completely. For this purpose, NAP−XPS experiments were performed on Pd/SOMS exposed to liquid ethanol. The excess ethanol was removed from the NAP−XPS chamber by heating at 60 °C. The spectra obtained over unswollen Pd/SOMS and Pd/SOMS exposed to ethanol are shown in Figure 6. The spectrum of Pd/SOMS shown in Figure 6a did not exhibit any Pd signals, as previously observed under vacuum. The spectrum of Pd/SOMS exposed to ethanol collected under the same scanning parameters, however, exhibited a Pd $3d_{5/2}$ and $3d_{3/2}$ doublet, indicating the presence of Pd NPs on the surface of the swollen Pd/SOMS. This clearly demonstrates that the accessibility of Pd particles deposited on SOMS scaffold increases in the presence of organics. The deconvolution of the spectrum was not performed due to low signal-to-noise ratio. There are three reasons why the obtained spectrum was noisy: (i) the extent to which Pd/SOMS is swollen during spectral acquisition may not be at its fullest since continuous evaporation of the solvent due to vacuum conditions may shrink Pd/SOMS, (ii) the amount of Pd in Pd/SOMS was one weight percent, approximately corresponding to 0.1 atomic percent. Therefore, the counts obtained due to Pd was expected to be low, and (iii) the design of in-house NAP−XPS with in situ investigation capabilities were only possible by placing an aperture at the end of the NAP−XPS reaction cell, resulting in smaller data collection area and low XPS counts.[45]

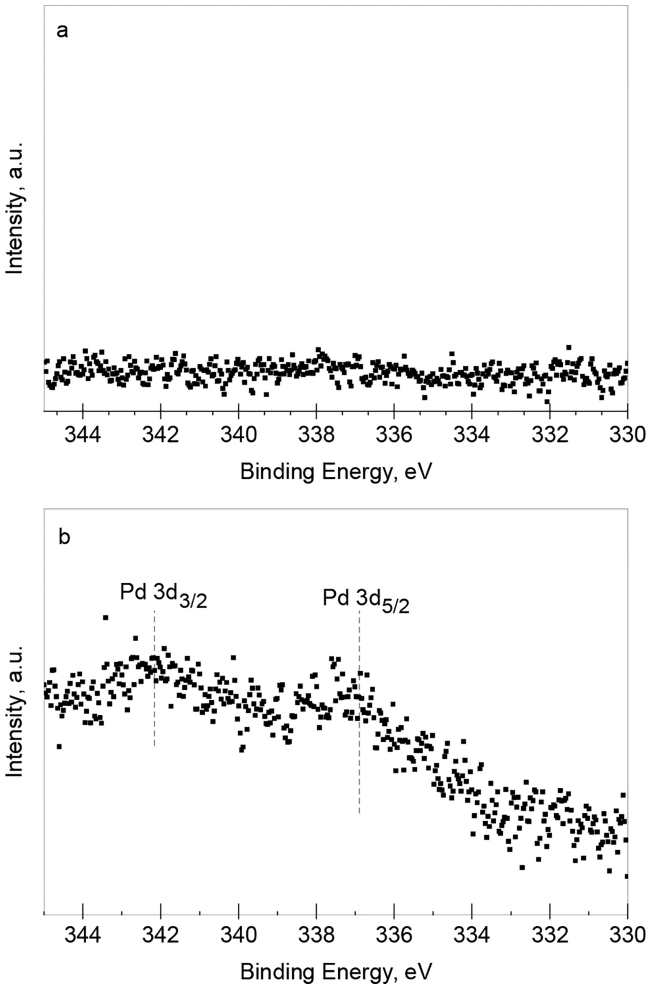

Figure 6. NAP−XPS Pd 3d region of (a) 1%Pd/SOMS and (b) 1% Pd/SOMS exposed to ethanol.

It is well-known that the catalytic surfaces are subject to change under reaction conditions. In certain cases, new active surfaces or sites may even be created.[45,71−73] This is actually one of the reasons why NAP−XPS is a powerful tool to characterize the catalyst surfaces under reaction conditions. What has been observed over Pd/SOMS, however, is not an example of such a change. Pd NPs became accessible on the surface of the catalyst after exposure to an organic compound. This indicates that the position of the active sites can be controlled by changing the reaction environment, resulting in achieving tunable accessibility of the active sites. It is still possible that, once Pd NPs are made accessible on the surface, the electronic and geometric structure of the Pd NPs may undergo some reaction-driven changes due to catalytic reactions, deactivation, or pretreatment operations. As long as such operations do not impair the swelling characteristics of the catalyst, removal of organic reaction environment will cause Pd/SOMS to shrink and return to its unswollen state where the active sites are kept inside the bulk of the matrix.

3.2.2. Cryogenic SEM over SOMS and Pd/SOMS. The morphological changes of SOMS scaffolds induced by swelling cannot be studied by conventional SEM because solvent

DOI: 10.1021/acscatal.8b01700
ACS Catal. 2018, 8, 6796−6809

evaporation takes place due to the high vacuum conditions required for imaging. SOMS scaffolds shrink and return to its unswollen state rapidly upon removal of the swelling agent.[11] In order to prevent the evaporation during imaging, SOMS and Pd-incorporated SOMS were studied by cryogenic SEM. The swelling was induced by exposure to a few drops of an organic swelling agent before samples were loaded into SEM cryo-preparation chamber. Ethylene glycol was used as a swelling agent because of its low vapor pressure compared to other organic swelling agents such as ethanol or acetone. The evaporation of the swelling agent was suppressed by keeping the samples at 133 K during imaging. This is a unique advantage of studying SOMS scaffolds in their swollen state by cryo-SEM, an advantage that cannot be achieved by conventional SEM.

Cryo-SEM micrographs collected over unswollen and swollen SOMS are shown in Figure 7a,b and 7c,d, respectively.

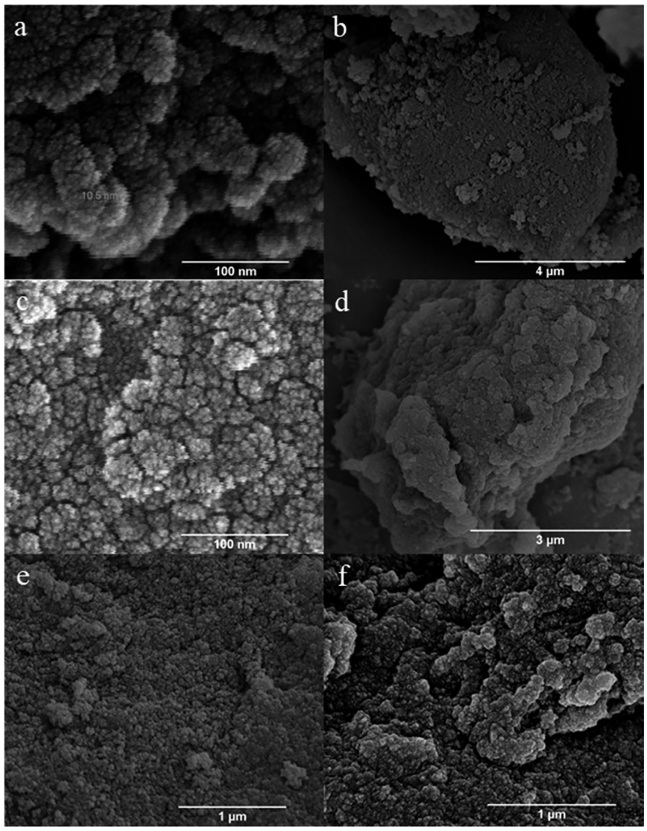

Figure 7. Cryo-SEM micrographs collected over (a and b) unswollen SOMS, and (c and d) swollen SOMS, (e) unswollen 1%Pd/SOMS, and (f) swollen 1%Pd/SOMS

SOMS in its unswollen state was found to be composed of approximately 25−30 nm sized particles clustered into small aggregates. The inspection of the structure of SOMS revealed the presence of large void spaces ranging from 10 to 70 nm. Void spaces in a size range of 10−20 nm were defined as complementary pores while larger void spaces were attributed to the spacing between clusters of SOMS particles. The pore sizes observed by SEM are in excellent agreement with the pore size distribution obtained from the BJH desorption branch of the isotherm presented in Figure 1a. It should be noted that the structural mesopores, observed through N_2 physisorption, having pore sizes less than 10 nm cannot be examined by SEM because of its resolution.[74] As also evidenced by the broad nature of the pore size distribution of SOMS, the absence of a well-ordered porous structure in SOMS can be seen from the images. The morphology of SOMS scaffold was found to be similar to the morphologies of other organosilicate materials prepared by sol−gel synthesis with a base catalysis or fluoride catalysis.[11,74−76]

The micrographs of swollen SOMS scaffolds show distinct changes on the morphology of SOMS scaffolds upon swelling. The most notable difference was the expansion of the SOMS matrix. The size and shape of SOMS particles, however, remained similar to that obtained over unswollen SOMS. This suggests that the particle sizes of aggregates of SOMS do not change markedly. A similar conclusion was also drawn by Burkett et al.[11] when SEM micrographs were obtained over swollen and partially swollen SOMS by critical point drying.

Cryo-SEM images of Pd-incorporated samples are shown in Figure 7e,f. The cryo-SEM micrograph of Pd/SOMS exhibited similar surface morphology to that of unswollen SOMS. The structure was composed of 25−30 nm sized particles clustered into small aggregates. One difference is, however, that large void spaces observed over SOMS was not present in Pd/SOMS. A similar result was also obtained by the pore size distribution shown in Figure 1a. It is anticipated that the complementary pores and interparticle void spaces were lost because of Pd impregnation. The micrograph of the swollen sample, shown in Figure 7f, also exhibited a physical expansion due to swelling.

It should be acknowledged that the degree of swelling may not be at its fullest because it is possible that some of the swelling agent evaporated during sample handling and imaging, although care was taken to obtain images as quickly as possible. Nevertheless, the series of images shown in the manuscript displays clear differences in morphologies of SOMS and Pd/SOMS due to swelling.

3.3. Aqueous-Phase HDC of TCE Catalytic Activity.

3.3.1. Aqueous-Phase HDC of TCE over 1%Pd/SOMS: Activity and Product Distribution. 1%Pd/SOMS was tested for aqueous-phase HDC of TCE at 30 °C and 50 bar. Prior to the reaction, 1%Pd/SOMS was reduced with $NaBH_4$. TCE conversion obtained over 1%Pd/SOMS with respect to time is shown in Figure 8a with error bars based on standard deviation. By the end of 40 min, 30% of TCE initially present in the reactor was converted. TCE conversions obtained at the end of 80 min and at the end of 6 h were 40% and 60%, respectively. The main chloride-containing product was found to be HCl with a selectivity of 91% indicating that HCl is the main chloride-containing reaction product. Throughout the reaction, partially chlorinated ethylenes including vinyl chloride, 1,1-dichloroethylene, trans-1,2-dichloroetylene, and cis-1,2-dichloroethylene were also observed with low selectivities as shown in Figure 8b. At the end of 6 h of reaction duration, the major side product was found to be cis-1,2-dichoroethylene with selectivity less than 5%. Selectivity values of the other chloride-containing side products were found to be zero at the end of 6 h. Selectivity results are important to demonstrate that TCE was converted to HCl without any build-up of partially dechlorinated products. It was reported that build-up of partially chlorinated side products with high yield values can be observed in other remediation techniques such as biologically mediated HDC and zerovalent iron dechlorination.[77]

DOI: 10.1021/acscatal.8b01700
ACS Catal. 2018, 8, 6796−6809

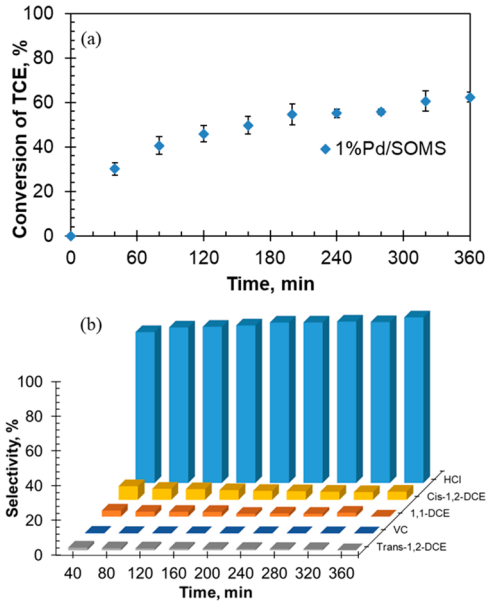

Figure 8. Catalytic activity data obtained over 1%Pd/SOMS at 50 bar, 30 °C, and 40 $mL_{solution}/mg_{catalyst}$ (a) TCE conversion and (b) selectivity of chloride-containing products with respect to the reaction time.

3.3.2. Aqueous-Phase HDC of TCE over 1%Pd/SOMS: Comparison to 1%Pd/Al_2O_3. Catalytic activity experiments in the batch-mode at 50 bar and 30 °C were performed over 1% Pd/SOMS and 1%Pd/Al_2O_3. Figure 9a shows that 1%Pd/Al_2O_3 exhibited a plateau-type catalytic activity before reaching 100% conversion and the rate of HDC became zero after 4.5 h. A first-order reaction such as HDC of TCE should reach complete conversion in a batch-reactor unless there is a deactivation and/or an inhibition effect.[24,78−80] Similar catalytic performances observed over 1%Pd/Al_2O_3 were reported in the literature and attributed to the inhibition due to the reaction product HCl.[52]

Although 1%Pd/SOMS exhibited lower catalytic activity than 1%Pd/Al_2O_3, the rate of HDC of TCE over 1%Pd/SOMS did not become zero. Continuous conversion of TCE was maintained during the course of the reaction experiment, indicating the absence of a complete deactivation effect due to HCl.

Although the rate of the reaction did not become zero over 1%Pd/SOMS, the catalytic activity may still be inhibited by chloride adsorption on the active sites. It is conceivable that chloride accumulation on the active sites may inhibit the catalytic performance if the reaction was continued further. It is also conceivable that the observed catalytic activity may be affected by the swellable nature of Pd/SOMS. Nevertheless, the results are significant in showing the higher inhibition resistance achieved over 1%Pd/SOMS in comparison with 1% Pd/Al_2O_3 under the same reaction conditions.

3.3.3. Aqueous-Phase HDC of TCE over Pd/SOMS and Pd/Al_2O_3: Experiments in the Presence of Ethanol. During HDC of TCE, the swelling of 1%Pd/SOMS is induced by the reactant TCE, which is also an organic swelling agent. It is conceivable that the degree to which 1%Pd/SOMS is swollen under reaction conditions changes throughout the reaction. In a batch reactor, as TCE gets converted to the HDC products, the total concentration of organics in the reaction medium decreases. As a result, 1%Pd/SOMS shrinks in a manner

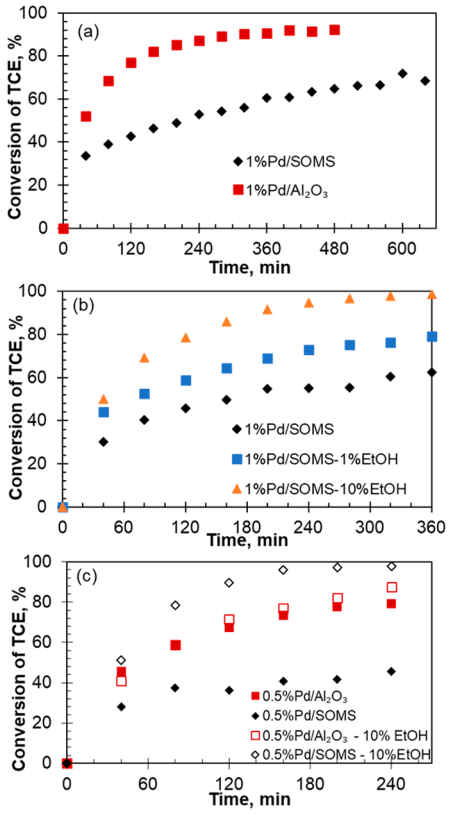

Figure 9. Catalytic activity data showing TCE conversions over (a) 1%Pd/SOMS and 1%Pd/Al_2O_3 at 50 bar, 30 °C, and 40 $mL_{solution}/mg_{catalyst}$, (b) 1%Pd/SOMS in absence and presence of 1% and 10% ethanol in the reaction mixture at 50 bar, 30 °C, and 40 $mL_{solution}/mg_{catalyst}$, (c) 0.5%Pd/SOMS and 0.5%Pd/Al_2O_3 in absence and presence of 10% ethanol in the reaction mixture at 30 bar, 30 °C, and 10 $mL_{solution}/mg_{catalyst}$.

dependent on the concentration of TCE.[9−11] This, in turn, changes the accessibility of Pd NPs that were deposited inside the swollen matrix, as evidenced by XPS, and were not accessible to reactants in the gas phase, as evidenced by CO pulse chemisorption. A strong evidence for variable accessibility of Pd NPs with respect to the reaction environment is presented in Section 3.2.1 by NAP−XPS. It is possible that the catalytic activity observed over Pd/SOMS could be controlled by the varied accessibility of Pd NPs throughout the reaction. To examine this phenomenon further, activity experiments were performed by varying the ethanol concentration. By using different concentrations of ethanol, it was aimed to maintain different extents of swelling of 1%Pd/SOMS matrix throughout the reaction. As shown in Figure 9b, TCE conversion obtained with 1%Pd/SOMS increased from 43% to 59% due to the presence of 1% ethanol and from 43% to 79% due to the presence of 10% ethanol in the reaction medium at the end of 120 min. With activity experiments performed in the presence of ethanol, three observations were made: (i) having ethanol in the reactor enhanced the observed catalytic activity of Pd/SOMS, (ii) the observed activity increased with increasing concentration of ethanol in the reaction medium, and (iii) the conversion reached 100% when 10% ethanol was present in the reactor and no plateau was observed.

Effect of ethanol was further examined by changing the reaction parameters, including Pd loading, pressure and reactant concentration, to ensure that the observed behavior

DOI: 10.1021/acscatal.8b01700
ACS Catal. 2018, 8, 6796−6809

was not limited to a specific set of parameters. Experiments were performed over 20 mg of 0.5%Pd/SOMS or 0.5%Pd/Al_2O_3 at 30 bar and 30 °C. It can be seen in Figure 9c that having ethanol in the reactor significantly increased the TCE conversion obtained over 0.5%Pd/SOMS. Presence of 10% ethanol in the reaction medium increased the TCE conversion from 42% to 97% at the end of 240 min of reaction duration.

When the effect of ethanol over 0.5%Pd/Al_2O_3 was examined (Figure 9c), there were no discernible differences in the TCE conversion whether the experiment was performed in the presence or absence of ethanol. This finding is important in showing that the enhancement effect of ethanol is unique to the Pd catalyst supported over SOMS and not a general promotional effect.

We attribute the positive effect of ethanol on the catalytic activity to the changes in the accessibility of the active sites due to swelling of Pd/SOMS. As the extent of swelling was increased by increasing the concentration of ethanol, more Pd NPs became accessible to participate in the reaction. This can be considered a "stimulus-induced response of the active sites" where the stimulus is the concentration of organic swelling agents.

An alternative explanation of the enhancement effect could be that ethanol may be facilitating the removal of HCl from the vicinity of the active sites. Chaplin et al. reported that if Pd-based catalysts are exposed to HCl at a concentration range of 700−2000 mol HCl/mol Pd during HDC, the catalyst inhibition occurred. At concentrations lower than the above-mentioned range, formation of HCl due to HDC did not result in inhibition.[25,36,52,81−85] Our batch reactor was operated under such conditions that, if there is an inhibition effect due to HCl, this effect could be experimentally observed. Since such an inhibition effect was not observed in the presence of ethanol, an activity increase due to more facile HCl removal remains a possibility. Although such an enhancement effect of ethanol was not observed over Pd/Al_2O_3, it should be noted that the Pd sites on the alumina support are primarily on the surface and the removal of HCl from the vicinity of the sites can be achieved more readily.

It should, however, also be noted that a similar enhancement effect of ethanol was reported when HCl inhibition was negligible in our previous work in the liquid phase.[18] Therefore, the observed activity increase achieved in the presence of ethanol in the reaction solution is more likely due to the enhanced accessibility of the active sites through swelling. However, a combined effect, that is, enhanced accessibility of the active sites and a more facile removal of the HCl from the vicinity of the active sites, cannot be ruled out.

Another important consideration about SOMS is its hydrophobicity. It is conceivable that SOMS support provide better resistance to poisons that are dissolved in water, by repelling water. Considering that the dispersion of Pd NPs is higher on Pd/Al_2O_3,[18] the higher activity observed over swollen Pd/SOMS in comparison to Pd/Al_2O_3 signals better resistance to HCl inhibition. Current efforts focus on exploring deactivation-resistant characteristics of Pd/SOMS against chloride and reduced sulfur species.

4. CONCLUSIONS

In this study, swellable organically modified silica was demonstrated to be a novel catalyst scaffold with unique characteristics for catalytic treatment of water contaminated with trichloroethylene. The swelling capability of SOMS allowed us to deposit Pd NPs inside the swollen matrix during synthesis, which was carried out in the presence of organic swelling agents. Pd NPs incorporated to SOMS exhibited a "stimulus-induced response of the active sites" where the stimulus is the concentration of organic swelling agents. Catalytic activity experiments performed in the presence of such agents (i.e., ethanol) showed that the catalytic performance improved with increasing concentration of the organic swelling agent. This behavior was attributed to the enhanced accessibility of the active sites due to swelling.

Having a supported catalyst with tunable accessibility of the active sites induced by changes in the reaction environment can have significant implications for heterogeneous catalysis. Such a behavior of active sites opens the possibility of using SOMS scaffolds for engineering "smart catalysts" for catalytic reactions where this characteristic can be utilized. This unique characteristic originates from the swellable nature of SOMS upon exposure to organics and incorporation of Pd NPs inside the swollen matrix of SOMS during synthesis. Therefore, swellable counterparts of the commonly used catalytic supports, such as alumina, ceria, zirconia, among others, may emerge as a new class of catalytic materials, particularly for catalytic water abatement. In addition, the need for more investigations is clear to elucidate the effect of swelling and stimuli-induced behavior of the active sites on the catalytic performance and to develop rate expressions in which the animated nature of SOMS is taken into account.

■ ASSOCIATED CONTENT

Supporting Information

The Supporting Information is available free of charge on the ACS Publications website at DOI: 10.1021/acscatal.8b01700.

Pd K-edge EXAFS fitting results for prereduction and postreduction samples, α_s-plot of SOMS, and adsorption of acetone and water on SOMS and 1%Pd/SOMS (PDF)

■ AUTHOR INFORMATION

Corresponding Author

*E-mail: ozkan.1@osu.edu. Tel: (614)-292-6623.

ORCID

Yu Tang: 0000-0001-9435-9310

Franklin Feng Tao: 0000-0002-4916-6509

Umit S. Ozkan: 0000-0001-5571-2257

Notes

The authors declare no competing financial interest.

■ ACKNOWLEDGMENTS

The financial support for this work was provided by the National Science Foundation through the Grant CBET-1436729 and Ohio Coal Research Consortium. The authors wish to thank Dr. Lisa Hommel and Dr. Daniel Huber for their valuable assistances in XPS data acquisition and SEM imaging, respectively. J.T.M. was supported as part of the National Science Foundation Energy Research Center for Innovative and Strategic Transformation of Alkane Resources (CISTAR) under the Cooperative Agreement No. EEC-1647722. Y.T. and F.T. were partially supported by the NSF Career Award NSF-CHE-14162121, and Chemical Sciences, Geosciences and Biosciences Division, Office of Basic Energy Sciences, Office of

DOI: 10.1021/acscatal.8b01700
ACS Catal. 2018, 8, 6796−6809

Science, U.S. Department of Energy under Grant No. DE-SC0014561. Electron microscopy was performed at the Center for Electron Microscopy and Analysis (CEMAS) at The Ohio State University. This study also made use of the Materials Research Collaborative Access Team's (MRCAT) sector 10-ID-B at Argonne National Laboratory. MRCAT operations are supported by the Department of Energy and the MRCAT member institutions. This research used resources of the Advanced Photon Source, a U.S. Department of Energy (DOE) Office of Science User Facility operated for the DOE Office of Science by Argonne National Laboratory under Contract No. DE-AC02-06CH11357.

REFERENCES

(1) Patel, V. R.; Amiji, M. M. pH-Sensitive Swelling and Drug-Release Properties of Chitosan—Poly(ethylene oxide) Semi-interpenetrating Polymer Network. In *Hydrogels and Biodegradable Polymers for Bioapplications*; Ottenbrite, R. M., Huang, S. J., Park, K., Eds.; American Chemical Society: Washington, DC, 1996; Vol. *627*, pp 209−220.

(2) Khalid, M. N.; Agnely, F.; Yagoubi, N.; Grossiord, J. L.; Couarraze, G. Water state characterization, swelling behavior, thermal and mechanical properties of chitosan based networks. *Eur. J. Pharm. Sci.* **2002**, *15*, 425−432.

(3) Elvira, C.; Mano, J. F.; San Román, J.; Reis, R. L. Starch-based biodegradable hydrogels with potential biomedical applications as drug delivery systems. *Biomaterials* **2002**, *23*, 1955−1966.

(4) Rao, M. S.; Gray, J.; Dave, B. C. Smart Glasses: Molecular Programming of Dynamic Responses in Organosilica Sol-Gels. *J. Sol-Gel Sci. Technol.* **2003**, *26*, 553−560.

(5) Rao, M.; Dave, B. C. Smart" Glasses: Molecular Programming of Rapid Dynamic Responses in Organosilica Sol−Gels. *Adv. Mater.* **2002**, *14*, 443−447.

(6) Rao, M.; Dave, B. C. Thermoresponsive Glasses: Temperature-Controlled Rapid Swelling and Deswelling of Silica-Based Sol−Gels. *Adv. Mater.* **2001**, *13*, 274−276.

(7) Davankov, V.; Tsyurupa, M. Structure and properties of hypercrosslinked polystyrene—the first representative of a new class of polymer networks. *React. Polym.* **1990**, *13*, 27−42.

(8) Tsyurupa, M.; Maslova, L.; Andreeva, A.; Mrachkovskaya, T.; Davankov, V. Sorption of organic compounds from aqueous media by hypercrosslinked polystyrene sorbents 'Styrosorbrs. *React. Polym.* **1995**, *25*, 69−78.

(9) Edmiston, P. L.; Underwood, L. A. Absorption of dissolved organic species from water using organically modified silica that swells. *Sep. Purif. Technol.* **2009**, *66*, 532−540.

(10) Burkett, C. M.; Edmiston, P. L. Highly swellable sol−gels prepared by chemical modification of silanol groups prior to drying. *J. Non-Cryst. Solids* **2005**, *351*, 3174−3178.

(11) Burkett, C. M.; Underwood, L. A.; Volzer, R. S.; Baughman, J. A.; Edmiston, P. L. Organic−Inorganic Hybrid Materials that Rapidly Swell in Non-Polar Liquids: Nanoscale Morphology and Swelling Mechanism. *Chem. Mater.* **2008**, *20*, 1312−1321.

(12) Tsyurupa, M. P.; Davankov, V. A. Porous structure of hypercrosslinked polystyrene: State-of-the-art mini-review. *React. Funct. Polym.* **2006**, *66*, 768−779.

(13) Tsyurupa, M. P.; Davankov, V. A. Hypercrosslinked polymers: basic principle of preparing the new class of polymeric materials. *React. Funct. Polym.* **2002**, *53*, 193−203.

(14) Canal, T.; Peppas, N. A. Correlation between mesh size and equilibrium degree of swelling of polymeric networks. *J. Biomed. Mater. Res.* **1989**, *23*, 1183−1193.

(15) Brannon-Peppas, L.; Peppas, N. A. Equilibrium swelling behavior of pH-sensitive hydrogels. *Chem. Eng. Sci.* **1991**, *46*, 715−722.

(16) Sohn, H.; Celik, G.; Gunduz, S.; Majumdar, S. S.; Dean, S. L.; Edmiston, P. L.; Ozkan, U. S. Effect of high-temperature on the swellable organically-modified silica (SOMS) and its application to gas-phase hydrodechlorination of trichloroethylene. *Appl. Catal., B* **2017**, *209*, 80−90.

(17) Celik, G.; Ailawar, S. A.; Gunduz, S.; Edmiston, P. L.; Ozkan, U. S. Formation of carbonaceous deposits on Pd-based hydrodechlorination catalysts: Vibrational spectroscopy investigations over Pd/Al2O3 and Pd/SOMS. *Catal. Today* **2018**, DOI: 10.1016/j.cattod.2018.05.001.

(18) Sohn, H.; Celik, G.; Gunduz, S.; Dean, S. L.; Painting, E.; Edmiston, P. L.; Ozkan, U. S. Hydrodechlorination of trichloroethylene over Pd supported on swellable organically-modified silica (SOMS). *Appl. Catal., B* **2017**, *203*, 641−653.

(19) Edmiston, P. L.; West, L. J.; Chin, A.; Mellor, N.; Barth, D. Adsorption of Gas Phase Organic Compounds by Swellable Organically Modified Silica. *Ind. Eng. Chem. Res.* **2016**, *55*, 12068−12079.

(20) Edmiston, P. L.; Gilbert, A. R.; Harvey, Z.; Mellor, N. Adsorption of short chain carboxylic acids from aqueous solution by swellable organically modified silica materials. *Adsorption* **2018**, *24*, 53−63.

(21) Khalid, M. N.; Agnely, F.; Yagoubi, N.; Grossiord, J. L.; Couarraze, G. Water state characterization, swelling behavior, thermal and mechanical properties of chitosan based networks. *Eur. J. Pharm. Sci.* **2002**, *15*, 425−432.

(22) Schreier, C. G.; Reinhard, M. Catalytic hydrodehalogenation of chlorinated ethylenes using palladium and hydrogen for the treatment of contaminated water. *Chemosphere* **1995**, *31*, 3475−3487.

(23) Nutt, M. O.; Hughes, J. B.; Wong, M. S. Designing Pd-on-Au Bimetallic Nanoparticle Catalysts for Trichloroethene Hydrodechlorination. *Environ. Sci. Technol.* **2005**, *39*, 1346−1353.

(24) Lowry, G. V.; Reinhard, M. Hydrodehalogenation of 1-to 3-carbon halogenated organic compounds in water using a palladium catalyst and hydrogen gas. *Environ. Sci. Technol.* **1999**, *33*, 1905−1910.

(25) Chaplin, B. P.; Reinhard, M.; Schneider, W. F.; Schuth, C.; Shapley, J. R.; Strathmann, T. J.; Werth, C. J. Critical Review of Pd-Based Catalytic Treatment of Priority Contaminants in Water. *Environ. Sci. Technol.* **2012**, *46*, 3655−3670.

(26) Ordóñez, S.; Díez, F. V.; Sastre, H. Catalytic Hydrodechlorination of Chlorinated Olefins over a Pd/Al2O3 Catalyst: Kinetics and Inhibition Phenomena. *Ind. Eng. Chem. Res.* **2002**, *41*, 505−511.

(27) Cobo, M.; González, C. A.; Sánchez, E. G.; Montes, C. Catalytic hydrodechlorination of trichloroethylene with 2-propanol over Pd/Al2O3. *Catal. Today* **2011**, *172*, 78−83.

(28) Cobo, M.; Becerra, J.; Castelblanco, M.; Cifuentes, B.; Conesa, J. A. Catalytic hydrodechlorination of trichloroethylene in a novel NaOH/2-propanol/methanol/water system on ceria-supported Pd and Rh catalysts. *J. Environ. Manage.* **2015**, *158*, 1−10.

(29) Sahu, R. S.; Li, D. L.; Doong, R. A. Unveiling the hydrodechlorination of trichloroethylene by reduced graphene oxide supported bimetallic Fe/Ni nanoparticles. *Chem. Eng. J.* **2018**, *334*, 30−40.

(30) Kaminska, II; Lisovytskiy, D.; Casale, S.; Srebowata, A.; Dzwigaj, S. Influence of preparation procedure on catalytic activity of PdBEA zeolites in aqueous phase hydrodechlorination of 1,1,2-trichloroethene. *Microporous Mesoporous Mater.* **2017**, *237*, 65−73.

(31) Han, Y. L.; Liu, C. J.; Horita, J.; Yan, W. L. Trichloroethene hydrodechlorination by Pd-Fe bimetallic nanoparticles: Solute-induced catalyst deactivation analyzed by carbon isotope fractionation. *Appl. Catal., B* **2016**, *188*, 77−86.

(32) Srebowata, A.; Tarach, K.; Girman, V.; Gora-Marek, K. Catalytic removal of trichloroethylene from water over palladium loaded microporous and hierarchical zeolites. *Appl. Catal., B* **2016**, *181*, 550−560.

(33) Lowry, G. V.; Reinhard, M. Pd-catalyzed TCE dechlorination in groundwater: Solute effects, biological control, and oxidative catalyst regeneration. *Environ. Sci. Technol.* **2000**, *34*, 3217−3223.

(34) Ordóñez, S.; Díez, F. V.; Sastre, H. Characterisation of the deactivation of platinum and palladium supported on activated carbon

DOI: 10.1021/acscatal.8b01700
ACS Catal. 2018, 8, 6796−6809

used as hydrodechlorination catalysts. *Appl. Catal., B* **2001**, *31*, 113−122.
(35) Ordóñez, S.; Sastre, H.; Díez, F. V. Thermogravimetric determination of coke deposits on alumina-supported noble metal catalysts used as hydrodechlorination catalysts. *Thermochim. Acta* **2001**, *379*, 25−34.
(36) Keane, M. A. Supported Transition Metal Catalysts for Hydrodechlorination Reactions. *ChemCatChem* **2011**, *3*, 800−821.
(37) Gampine, A.; Eyman, D. P. Catalytic Hydrodechlorination of Chlorocarbons. 2. Ternary Oxide Supports for Catalytic Conversions of 1,2-Dichlorobenzene. *J. Catal.* **1998**, *179*, 315−325.
(38) Gopinath, R.; Lingaiah, N.; Sreedhar, B.; Suryanarayana, I.; Sai Prasad, P. S.; Obuchi, A. Highly stable Pd/CeO2 catalyst for hydrodechlorination of chlorobenzene. *Appl. Catal., B* **2003**, *46*, 587−594.
(39) Coq, B. Conversion Under Hydrogen of Dichlorodifluoromethane over Supported Palladium Catalysts. *J. Catal.* **1993**, *141*, 21−33.
(40) Coq, B. Conversion of chlorobenzene over palladium and rhodium catalysts of widely varying dispersion. *J. Catal.* **1986**, *101*, 434−445.
(41) López, E.; Ordóñez, S.; Sastre, H.; Dı, x.; ez, F. V. Kinetic study of the gas-phase hydrogenation of aromatic and aliphatic organochlorinated compounds using a Pd/Al2O3 catalyst. *J. Hazard. Mater.* **2003**, *97*, 281−294.
(42) Comandella, D.; Woszidlo, S.; Georgi, A.; Kopinke, F.-D.; Mackenzie, K. Efforts for long-term protection of palladium hydrodechlorination catalysts. *Appl. Catal., B* **2016**, *186*, 204−211.
(43) Hildebrand, H.; Mackenzie, K.; Kopinke, F. D. Pd/Fe3O4 nano-catalysts for selective dehalogenation in wastewater treatment processes-Influence of water constituents. *Appl. Catal., B* **2009**, *91*, 389−396.
(44) Jaroniec, M.; Kruk, M.; Olivier, J. P. Standard nitrogen adsorption data for characterization of nanoporous silicas. *Langmuir* **1999**, *15*, 5410−5413.
(45) Tao, F. Design of an in-house ambient pressure AP-XPS using a bench-top X-ray source and the surface chemistry of ceria under reaction conditions. *Chem. Commun.* **2012**, *48*, 3812−3814.
(46) Shan, J.-j.; Nguyen, L.; Zhang, S.; Tao, F.-F. Water−Gas Shift on Pd/α-MnO2 and Pt/α-MnO2. *Catal. Lett.* **2015**, *145*, 1571−1580.
(47) Sohn, H.; Celik, G.; Gunduz, S.; Dogu, D.; Zhang, S. R.; Shan, J. J.; Tao, F. F.; Ozkan, U. S. Oxygen Mobility in Pre-Reduced Nano- and Macro-Ceria with Co Loading: An AP-XPS, In-Situ DRIFTS and TPR Study. *Catal. Lett.* **2017**, *147*, 2863−2876.
(48) Kispersky, V. F.; Kropf, A. J.; Ribeiro, F. H.; Miller, J. T. Low absorption vitreous carbon reactors for operandoXAS: a case study on Cu/Zeolites for selective catalytic reduction of NO_x by NH_3. *Phys. Chem. Chem. Phys.* **2012**, *14*, 2229−2238.
(49) Langland, B. R.; Ribeiro, F. H.; Miller, J. T. Simultaneous Measurement of X-ray Absorption Spectra and Kinetics: A Fixed-bed, Plug-flow Operando Reactor. *Catal. Lett.* **2009**, *131*, 1−6.
(50) Ravel, B.; Newville, M. ATHENA, ARTEMIS, HEPHAESTUS: data analysis for X-ray absorption spectroscopy using IFEFFIT. *J. Synchrotron Radiat.* **2005**, *12*, 537−541.
(51) Ressler, T. WinXAS: A new software package not only for the analysis of energy-dispersive XAS data. *J. Phys. IV* **1997**, *7*, 269−270.
(52) Ordonez, S.; Vivas, B. P.; Diez, F. V. Minimization of the deactivation of palladium catalysts in the hydrodechlorination of trichloroethylene in wastewaters. *Appl. Catal., B* **2010**, *95*, 288−296.
(53) Fuertes, A. B.; Pico, F.; Rojo, J. M. Influence of pore structure on electric double-layer capacitance of template mesoporous carbons. *J. Power Sources* **2004**, *133*, 329−336.
(54) Fuertes, A. B.; Nevskaia, D. M. Control of mesoporous structure of carbons synthesised using a mesostructured silica as template. *Microporous Mesoporous Mater.* **2003**, *62*, 177−190.
(55) Sing, K. S. W. Reporting physisorption data for gas/solid systems with special reference to the determination of surface area and porosity (Recommendations 1984). *Pure Appl. Chem.* **1985**, *57*, 603−619.
(56) On, D. T.; Zaidi, S. M. J.; Kaliaguine, S. Stability of mesoporous aluminosilicate MCM-41 under vapor treatment, acidic and basic conditions. *Microporous Mesoporous Mater.* **1998**, *22*, 211−224.
(57) Chen, H. X.; Wang, Y. C. Preparation of MCM-41 with high thermal stability and complementary textural porosity. *Ceram. Int.* **2002**, *28*, 541−547.
(58) Groen, J. C.; Peffer, L. A. A.; Pérez-Ramírez, J. Pore size determination in modified micro- and mesoporous materials. Pitfalls and limitations in gas adsorption data analysis. *Microporous Mesoporous Mater.* **2003**, *60*, 1−17.
(59) Monteiro, R. S.; Dieguez, L. C.; Schmal, M. The role of Pd precursors in the oxidation of carbon monoxide over Pd/Al2O3 and Pd/CeO2/Al2O3 catalysts. *Catal. Today* **2001**, *65*, 77−89.
(60) Craciun, R.; Daniell, W.; Knozinger, H. The effect of CeO2 structure on the activity of supported Pd catalysts used for methane steam reforming. *Appl. Catal., A* **2002**, *230*, 153−168.
(61) Esteves, L. M.; Brijaldo, M. H.; Passos, F. B. Decomposition of acetic acid for hydrogen production over Pd/Al2O3 and Pd/TiO2: Influence of metal precursor. *J. Mol. Catal. A: Chem.* **2016**, *422*, 275−288.
(62) Bertarione, S.; Prestipino, C.; Groppo, E.; Scarano, D.; Spoto, G.; Zecchina, A.; Pellegrini, R.; Leofanti, G.; Lamberti, C. Direct IR observation of vibrational properties of carbonyl species formed on Pd nano-particles supported on amorphous carbon: comparison with Pd/SiO2-Al2O3. *Phys. Chem. Chem. Phys.* **2006**, *8*, 3676−3681.
(63) Huang, J.; Jiang, Y. J.; van Vegten, N.; Hunger, M.; Baiker, A. Tuning the support acidity of flame-made Pd/SiO2-Al2O3 catalysts for chemoselective hydrogenation. *J. Catal.* **2011**, *281*, 352−360.
(64) Sheu, L. L.; Karpinski, Z.; Sachtler, W. M. H. Effects of palladium particle size and palladium silicide formation on Fourier transform infrared spectra and carbon monoxide adsorbed on palladium/silicon dioxide catalysts. *J. Phys. Chem.* **1989**, *93*, 4890−4894.
(65) Pawelec, B.; Mariscal, R.; Navarro, R. M.; van Bokhorst, S.; Rojas, S.; Fierro, J. L. G. Hydrogenation of aromatics over supported Pt-Pd catalysts. *Appl. Catal., A* **2002**, *225*, 223−237.
(66) Tessier, D.; Rakai, A.; Bozonverduraz, F. Spectroscopic study of the interaction of carbon monoxide with cationic and metallic palladium in palladium−alumina catalysts. *J. Chem. Soc., Faraday Trans.* **1992**, *88*, 741−749.
(67) Moulder, J. F.; Chastain, J. *Handbook of X-ray Photoelectron Spectroscopy: A Reference Book of Standard Spectra for Identification and Interpretation of XPS Data*; Physical Electronics Division, Perkin-Elmer Corporation, 1992.
(68) Tew, M. W.; Miller, J. T.; van Bokhoven, J. A. Particle Size Effect of Hydride Formation and Surface Hydrogen Adsorption of Nanosized Palladium Catalysts: L-3 Edge vs K Edge X-ray Absorption Spectroscopy. *J. Phys. Chem. C* **2009**, *113*, 15140−15147.
(69) McCaulley, J. A. In-situ x-ray absorption spectroscopy studies of hydride and carbide formation in supported palladium catalysts. *J. Phys. Chem.* **1993**, *97*, 10372−10379.
(70) Miller, J. T.; Kropf, A. J.; Zha, Y.; Regalbuto, J. R.; Delannoy, L.; Louis, C.; Bus, E.; van Bokhoven, J. A. The effect of gold particle size on Au-Au bond length and reactivity toward oxygen in supported catalysts. *J. Catal.* **2006**, *240*, 222−234.
(71) Tao, F.; Grass, M. E.; Zhang, Y. W.; Butcher, D. R.; Renzas, J. R.; Liu, Z.; Chung, J. Y.; Mun, B. S.; Salmeron, M.; Somorjai, G. A. Reaction-Driven Restructuring of Rh-Pd and Pt-Pd Core-Shell Nanoparticles. *Science* **2008**, *322*, 932−934.
(72) Tao, F.; Dag, S.; Wang, L. W.; Liu, Z.; Butcher, D. R.; Bluhm, H.; Salmeron, M.; Somorjai, G. A. Break-Up of Stepped Platinum Catalyst Surfaces by High CO Coverage. *Science* **2010**, *327*, 850−853.
(73) Tao, F.; Salmeron, M. In Situ Studies of Chemistry and Structure of Materials in Reactive Environments. *Science* **2011**, *331*, 171−174.
(74) Kurumada, K.-i.; Nakabayashi, H.; Murataki, T.; Tanigaki, M. Structure and formation process of silica microparticles and monolithic gels prepared by the sol-gel method. *Colloids Surf., A* **1998**, *139*, 163−170.

DOI: 10.1021/acscatal.8b01700
ACS Catal. 2018, 8, 6796−6809

(75) Reale, E.; Leyva, A.; Corma, A.; Martinez, C.; Garcia, H.; Rey, F. A fluoride-catalyzed sol-gel route to catalytically active non-ordered mesoporous silica materials in the absence of surfactants. *J. Mater. Chem.* **2005**, *15*, 1742−1754.
(76) Cerveau, G.; Corriu, R. J. P.; Fischmeister-Lepeytre, C. Influence of kinetic parameters on the textural and chemical properties of silsesquioxane materials obtained by sol-gel process. *J. Mater. Chem.* **1999**, *9*, 1149−1154.
(77) Wong, M. S.; Alvarez, P. J. J.; Fang, Y. L.; Akcin, N.; Nutt, M. O.; Miller, J. T.; Heck, K. N. Cleaner water using bimetallic nanoparticle catalysts. *J. Chem. Technol. Biotechnol.* **2009**, *84*, 158−166.
(78) Nutt, M. O.; Heck, K. N.; Alvarez, P.; Wong, M. S. Improved Pd-on-Au bimetallic nanoparticle catalysts for aqueous-phase trichloroethene hydrodechlorination. *Appl. Catal., B* **2006**, *69*, 115−125.
(79) Fang, Y.-L.; Miller, J. T.; Guo, N.; Heck, K. N.; Alvarez, P. J. J.; Wong, M. S. Structural analysis of palladium-decorated gold nanoparticles as colloidal bimetallic catalysts. *Catal. Today* **2011**, *160*, 96−102.
(80) Pretzer, L. A.; Song, H. J.; Fang, Y.-L.; Zhao, Z.; Guo, N.; Wu, T.; Arslan, I.; Miller, J. T.; Wong, M. S. Hydrodechlorination catalysis of Pd-on-Au nanoparticles varies with particle size. *J. Catal.* **2013**, *298*, 206−217.
(81) Keane, M. A. A review of catalytic approaches to waste minimization: case study—liquid-phase catalytic treatment of chlorophenols. *J. Chem. Technol. Biotechnol.* **2005**, *80*, 1211−1222.
(82) Yuan, G.; Keane, M. A. Catalyst deactivation during the liquid phase hydrodechlorination of 2,4-dichlorophenol over supported Pd: influence of the support. *Catal. Today* **2003**, *88*, 27−36.
(83) Yuan, G.; Keane, M. A. Liquid phase hydrodechlorination of chlorophenols over Pd/C and Pd/Al2O3: a consideration of HCl/catalyst interactions and solution pH effects. *Appl. Catal., B* **2004**, *52*, 301−314.
(84) de Pedro, Z. M.; Diaz, E.; Mohedano, A. F.; Casas, J. A.; Rodriguez, J. J. Compared activity and stability of Pd/Al2O3 and Pd/AC catalysts in 4-chlorophenol hydrodechlorination in different pH media. *Appl. Catal., B* **2011**, *103*, 128−135.
(85) Shindler, Y.; Matatov-Meytal, Y.; Sheintuch, M. Wet Hydrodechlorination of p-Chlorophenol Using Pd Supported on an Activated Carbon Cloth. *Ind. Eng. Chem. Res.* **2001**, *40*, 3301−3308.

DOI: 10.1021/acscatal.8b01700
ACS Catal. 2018, 8, 6796−6809